Optical and radiometric models of the NOMAD instrument part II: the infrared channels - SO and LNO

I. R. Thomas,[1,*] A.C. Vandaele,[1] S. Robert,[1] E. Neefs,[1] R. Drummond,[1,2] F. Daerden,[1] S. Delanoye,[1] B. Ristic,[1] S. Berkenbosch,[1] R. Clairquin,[1] J. Maes,[1] S. Bonnewijn,[1] C. Depiesse,[1] A. Mahieux,[1,3] L. Trompet,[1] L. Neary,[1] Y. Willame,[1] V. Wilquet,[1] D. Nevejans,[1] L. Aballea,[4] W. Moelans,[4] L. De Vos,[4] S. Lesschaeve,[4] N. Van Vooren,[4] J.-J. Lopez-Moreno,[5] M. R. Patel,[6,8] G. Bellucci[7] and the NOMAD Team[†]

[1]Belgian Institute for Space Aeronomy (IASB-BIRA), 3 av Circulaire, 1180 Brussels, Belgium
[2]IndoSpace Ltd., 6 Nuneham Square, Abingdon,Oxon, OX14 1EH, UK
[3]Fonds National de la Recherche Scientifique, Brussels, Belgium
[4]OIP, Westerring 21, 9700 Oudenaarde, Belgium
[5]Instituto de Astrofisica de Andalucia (IAA/CSIC), 18080 Granada, Spain
[6]The Open University, Walton Hall, Milton Keynes, MK7 6AA, UK
[7]Istituto di Astrofisica e Planetologia Spaziali (IAPS/INAF), 00133, Rome, Italy
[8]Rutherford Appleton Laboratory, Oxfordshire, UK
[*]ian.thomas@aeronomie.be

Abstract: NOMAD is a suite of three spectrometers that will be launched in 2016 as part of the joint ESA-Roscosmos ExoMars Trace Gas Orbiter mission. The instrument contains three channels that cover the IR and UV spectral ranges and can perform solar occultation, nadir and limb observations, to detect and map a wide variety of Martian atmospheric gases and trace species. Part I of this work described the models of the UVIS channel; in this second part, we present the optical models representing the two IR channels, SO (Solar Occultation) and LNO (Limb, Nadir and Occultation), and use them to determine signal to noise ratios (SNRs) for many expected observational cases. In solar occultation mode, both the SO and LNO channel exhibit very high SNRs >5000. SNRs of around 100 were found for the LNO channel in nadir mode, depending on the atmospheric conditions, Martian surface properties, and observation geometry.

OCIS codes: (010.0280) Remote sensing and sensors; (120.6085) Space instrumentation; (120.6200) Spectrometers and spectroscopic instrumentation; (010.1280) Atmospheric composition; (010.5620) Radiative transfer.

References and links

1. A. C. Vandaele, Y. Willame, C. Depiesse, I. R. Thomas, S. Robert, D. Bolsée, M. R. Patel, J. P. Mason, M. Leese, S. Lesschaeve, P. Antoine, F. Daerden, S. Delanoye, R. Drummond, E. Neefs, B. Ristic, J. J. Lopez-Moreno, G. Bellucci, and N. Team, and the NOMAD Team, "Optical and Radiometric Models of the NOMAD Instrument Part I: The UVIS channel," Opt. Express **23**(23), 30028–30042 (2015).
2. D. Nevejans, E. Neefs, E. Van Ransbeeck, S. Berkenbosch, R. Clairquin, L. De Vos, W. Moelans, S. Glorieux, A. Baeke, O. Korablev, I. Vinogradov, Y. Kalinnikov, B. Bach, J.-P. Dubois, and E. Villard, "Compact high-resolution spaceborne echelle grating spectrometer with acousto-optical tunable filter based order sorting for the infrared domain from 2.2 to 4.3 μrm," Appl. Opt. **45**(21), 5191–5206 (2006).
3. J. L. Bertaux, D. Nevejans, O. Korablev, E. Villard, E. Quémerais, E. Neefs, F. Montmessin, F. Leblanc, J.-P. Dubois, E. Dimarellis, A. Hauchecorne, F. Lefevre, P. Rannou, J. Y. Chaufray, M. Cabane, G. Cernogora, G. Souchon, F. Semelina, A. Reberac, E. Van Ransbeek, S. Berkenbosch, R. Clairquin, C. Muller, F. Forget, F. Hourdin, O. Talagrand, A. Rodin, A. Fedorova, A. Stepanov, A. Vinogradov, A. Kiselev, Y. Kalinnikov, G. Durry, B. Sandel, A. Stern, and J. C. Gérard, "SPICAV on Venus Express: Three spectrometers to study the global structure and composition of the Venus atmosphere," Planet. Space Sci. **55**, 1673–1700 (2007).
4. H. Svedhem, D. Titov, D. McCoy, J.-P. Lebreton, S. Barabash, J. L. Bertaux, P. Drossart, V. Formisano, B. Häusler, O. Korablev, W. J. Markiewicz, D. Nevejans, M. Pätzold, G. Piccioni, T. L. Zhang, F. W. Taylor, E. Lellouch, D. Koschny, O. Witasse, H. Eggel, M. Warhaut, A. Accomazzo, J. Rodriguez-Canabal, J. Fabrega, T.

#252874 Received 29 Oct 2015; revised 7 Jan 2016; accepted 8 Jan 2016; published 16 Feb 2016

Shirmann, A. Clochet, and M. Coradini, "Venus Express: The first European mission to Venus," Planet. Space Sci. **55**, 1636–1652 (2007).
5. E. Neefs, A. C. Vandaele, R. Drummond, I. R. Thomas, S. Berkenbosch, R. Clairquin, S. Delanoye, B. Ristic, J. Maes, S. Bonnewijn, G. Pieck, E. Equeter, C. Depiesse, F. Daerden, E. V. Ransbeeck, D. Nevejans, J. Rodriguez-Gómez, J.-J. López-Moreno, R. Sanz, R. Morales, G. P. Candini, M. C. Pastor-Morales, B. Aparicio del Moral, J.-M. Jeronimo-Zafra, J. M. Gómez-López, G. Alonso-Rodrigo, I. Pérez-Grande, J. Cubas, A. M. Gomez-Sanjuan, F. Navarro-Medina, T. Thibert, M. R. Patel, G. Bellucci, L. De Vos, S. Lesschaeve, N. V. Vooren, W. Moelans, L. Aballea, S. Glorieux, A. Baeke, D. Kendall, J. De Neef, A. Soenen, P.-Y. Puech, J. Ward, J.-F. Jamoye, D. Diez, A. Vicario-Arroyo, and M. Jankowski, "NOMAD spectrometer on the ExoMars trace gas orbiter mission: part 1--design, manufacturing and testing of the infrared channels," Appl. Opt. **54**(28), 8494–8520 (2015).
6. R. Drummond, A. C. Vandaele, F. Daerden, D. Fussen, A. Mahieux, L. Neary, E. Neefs, S. Robert, Y. Willame, and V. Wilquet, "Studying methane and other trace species in the Mars atmosphere using a SOIR instrument," Planet. Space Sci. **59**(2), 292–298 (2011).
7. A. C. Vandaele, M. De Mazière, R. Drummond, A. Mahieux, E. Neefs, V. Wilquet, O. Korablev, A. Fedorova, D. Belyaev, F. Montmessin, and J. L. Bertaux, "Composition of the Venus mesosphere measured by Solar Occultation at Infrared on board Venus Express," J. Geophys. Res. **113**, E00B23 (2008).
8. S. Vandenbussche, S. Kochenova, A. C. Vandaele, N. Kumps, and M. De Maziere, "Retrieval of desert dust aerosol vertical profiles from IASI measurements in the TIR atmospheric window," Atmos. Meas. Tech. **6**(10), 2577–2591 (2013).
9. J. Bell III, M. Wolff, T. C. Daley, D. Crisp, P. B. James, S. W. Lee, J. T. Trauger, and R. W. Evans, "Near-Infrared Imaging of Mars from HST: Surface Reflectance, Photometric Properties, and Implications for MOLA Data," Icarus **138**, 25–35 (1999).
10. S. Robert, A. C. Vandaele, I. R. Thomas, Y. Willame, F. Daerden, S. Delanoye, C. Depiesse, R. Drummond, E. Neefs, L. Neary, B. Ristic, J-J. Lopez-Moreno, J. Rodriguez-Gomez, M. R. Patel, G. Bellucci, and the NOMAD Team are preparing a manuscript to be called "Expected Performances of the NOMAD/ExoMars instrument".

1. Introduction

NOMAD (Nadir and Occultation for MArs Discovery) is one of four instruments on board the ExoMars Trace Gas Orbiter that will observe the Martian atmosphere across a wide spectral range spanning the UV and IR spectral ranges. Part I of this work was dedicated to the UV-visible channel (200-650nm), known as UVIS, describing in detail the instrument and radiometric model [1]. This second part focuses on the two IR channels of the instrument, SO and LNO.

The design of the SO channel has been inspired by the existing spectrometer, SOIR [2], which was part of the SPICAV/SOIR spectrometers' suite [3] on board Venus-Express [4]. The SO channel has been optimized for solar occultation observations, i.e. looking at the Sun during sunset and sunrise. It operates at wavelengths between 2.2 and 4.3 μm (2325 to 4545 cm^{-1}) with a spectral resolution varying between 0.15 and 0.2 cm^{-1} depending on the wavelength region. The optical layout of LNO is identical to that of SO: radiation passes through the entrance optics, followed by the Acousto Optical Tunable Filter (AOTF), then slit, echelle spectrometer and is converted to an electronic signal by the cooled detector [Fig. 1]. LNO will be measuring in the wavelength range between 2.2 and 3.8 μm (2631 to 4545 cm^{-1}) with a resolution of ~0.3 cm^{-1}.

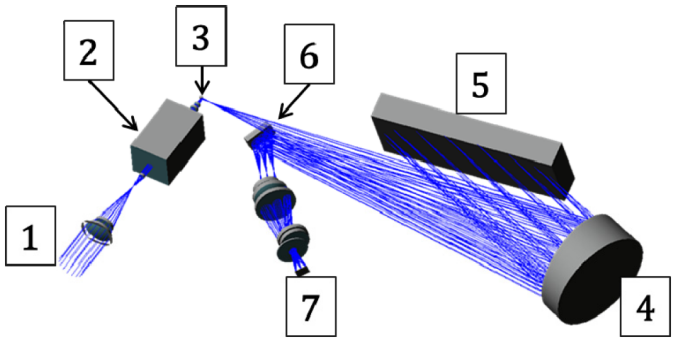

Fig. 1. Optical design of the SO and LNO channels: (1) the entrance optics, (2) the AOTF filter, (3) the spectrometer entrance slit, (4) collimating/imaging parabolic mirror, (6) folding mirror, (5) the echelle grating, (7) the detector.

#252874 Received 29 Oct 2015; revised 7 Jan 2016; accepted 8 Jan 2016; published 16 Feb 2016

The LNO channel contains a flip mirror that can be placed in one of two positions. When in nadir position, the channel field of view (FOV) is deflected downwards toward the centre of Mars, and when in occultation position, the mirror is no longer in the optical path and the FOV points directly towards the Sun, co-aligned with the SO channel. In both channels, the AOTF is used to select the spectral interval that will be recorded. In optimal conditions, its bandwidth should correspond exactly to the Free Spectral Range (FSR) of the spectrometer, so that the width of one AOTF diffraction order corresponds exactly with that of one echelle grating order. In practice, the FSR of the grating is constant in wavelength, and the AOTF bandwidth is constant in wavenumbers (inverse centimetres), so there is some mismatch across the spectral range of NOMAD. The detectors in both IR channels contain 320 columns (spectral direction) by 256 rows (spatial direction) of pixels, made of photovoltaic mercury cadmium telluride (HgCdTe/MCT) by Sofradir, France. These MARS-MW type detectors are cooled to a constant temperature, generally set in the range 80-100 K, during observations. More technical details on the NOMAD instrument and in particular on the IR channels can be found in [5].

2. Model parameters

2.1. Measurement cycles

For both channels, up to six different domains (corresponding to six different settings, or frequencies, of the AOTF) can be consecutively measured during each cycle, where one cycle typically lasts 1 s for solar occultation and 15 s for nadir observations - corresponding in nadir to a groundtrack footprint of approximately 17 × 50km from an orbit of 400km above Mars. As the instrument is highly programmable, many of the observational parameters can be varied depending on the state of the instrument and the conditions of the Martian atmosphere, and can be refined when in orbit around Mars. Therefore, for this work, the default parameters have been used, where six domains (i.e. 6 different diffraction orders) are measured per 1s cycle in occultation mode, and one domain (diffraction order) is measured per 15s cycle in nadir mode. Diffraction orders ~100-210 can typically be measured by SO; orders ~110-210 can be measured by LNO.

2.2. Operational temperatures

The NOMAD instrument has an expected operational temperature lying within 263-293K, calculated from thermal models. The resulting temperatures depend on several key factors which will change throughout the mission lifetime on variable time scales, such as: spacecraft temperature, Martian albedo, orbit altitude and beta angle, Mars' night side temperature, and degradation of the radiator emissivity over time. To reduce computational time and complexity, two models were run; one using all the best-case values (including significant negative margins) of each factor above, and one using all the worst-case values (with margins). We would expect the normal operational temperature to always be within the 263-293K range, but towards the lower end for a number of reasons: (1) degradation of the radiator's surface properties will only occur towards the end of the mission, (2) the spacecraft payload deck's worst-case temperature, with margin, is very high (>320K), and completely dominates the temperature of NOMAD, and (3) if, on the rare occasion that these worst-case values all happen to coincide, we have the option to switch off the instrument for certain orbits, or to reduce the duty cycle (e.g. shorten the nadir or occultation observations), as it is scientifically preferable to reduce the instrument temperature at the expense of global coverage. Hence, for this study, three instrument temperatures were chosen: 263K, 273K and 283K.

2.3. Effects of the Mars environment

The atmospheric and surface conditions of Mars, and the Mars-Sun distance and geometry also influence the results. The LNO nadir channel works by observing solar radiation reflected from the surface, and hence all of these factors affect the flux entering NOMAD,

#252874 Received 29 Oct 2015; revised 7 Jan 2016; accepted 8 Jan 2016; published 16 Feb 2016

changing the calculated SNR. The SO and LNO solar occultation channels work by viewing the Sun through the atmosphere of Mars – and are therefore not affected by surface properties or geometry, and have very high SNRs independent of the conditions when viewing the Sun. For the occultation calculations, the solar irradiance spectrum was taken from the "2000 Standard Extraterrestrial Spectrum Reference E-490-00" calculated by the American Society for Testing and Materials, a part of the National Renewable Energy Laboratory of the U.S. Department of Energy.

48 different conditions, in Table 1, were simulated for the geometry of the LNO channel when viewing nadir, using a full scattering scheme adapted to Martian conditions [6–8]. The model includes Rayleigh scattering, but not the absorption lines of the gas species that NOMAD is designed to measure. Aerosols properties (i.e. single scattering albedo, optical depth and aerosol scattering matrix provided as Legendre polynomials) are wavelength-dependent. The Sun irradiance has been considered here as a blackbody at the temperature of 5967K, the value most compatible with recent SOLSPEC observations [1]. The surface is considered to be Lambertian, characterized by a constant, wavelength-independent, albedo. Albedo values were chosen based on the compilation of [9]: 0.361 for bright regions, 0.179 for dark areas, and 0.242 as an intermediate value. For occultation viewing modes, reduction in optical transmission due to dust was not investigated. Note also that the Sun-Mars distance does not change the SNR in occultation mode, only the number of illuminated pixels.

Table 1. LNO nadir environmental parameters

Sun-Mars Distance (AU)	Surface Albedo [9]	Dust Optical Depth (OD)	Solar Zenith Angle (sza) (degrees)
1.38 (at perihelion, when L_S = 251°)	0.179 (Dark spots)	0.2	0, 45, 65, 80
		0.1,0.4, 0.7, 1.0	45
	0.242 (Intermediate value)	0.2	0, 45, 65, 80
		0.1,0.4, 0.7, 1.0	45
	0.361 (Bright spots)	0.2	0, 45, 65, 80
		0.1,0.4, 0.7, 1.0	45
1.67 (at aphelion, when L_S = 71°)	0.179 (Dark spots)	0.2	0, 45, 65, 80
		0.1,0.4, 0.7, 1.0	45
	0.242 (Intermediate value)	0.2	0, 45, 65, 80
		0.1,0.4, 0.7, 1.0	45
	0.361 (Bright spots)	0.2	0, 45, 65, 80
		0.1,0.4, 0.7, 1.0	45

3. Radiometric models of the SO and LNO channels

Radiometric models consist in general of two elements: (1) a simulation of the detected signal during one observation, considering the incoming radiation from the various environmental conditions (Table 1), and the attenuation of this signal due to the different optical components; (2) an estimation of the detector noise for that observation. From these quantities, signal to noise ratios (SNRs) can be calculated for each detector pixel *i* as follows:

$$SNR(i) = \frac{S(i)}{N(i)} \tag{1}$$

where *S(i)* is the signal and *N(i)* is the noise on pixel *i* during a single observation. The procedures for calculating these values are described in the following sections.

#252874 Received 29 Oct 2015; revised 7 Jan 2016; accepted 8 Jan 2016; published 16 Feb 2016

Photon flux entering the instrument

The spectral radiances for the various environmental scenarios described previously are shown in Fig. 2 and Fig. 3.

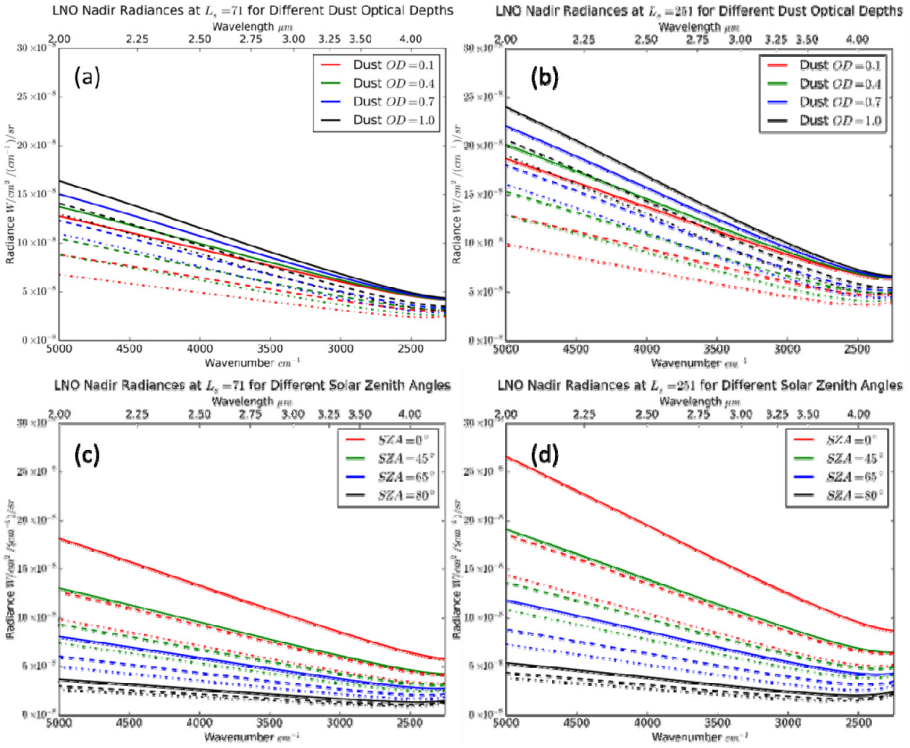

Fig. 2. Spectral radiances entering the LNO nadir aperture for the various cases described previously. They correspond to two different Sun-Mars distances: aphelion in (a) and (c), and perihelion in (b) and (d); for different dust opacities at a fixed sza of 45° (a) and (b), and different solar zenith angles for a fixed dust OD of 0.2 (c) and (d). Solid, dotted and dashed lines correspond to the different albedos (bright spots, intermediate, and dark areas respectively).

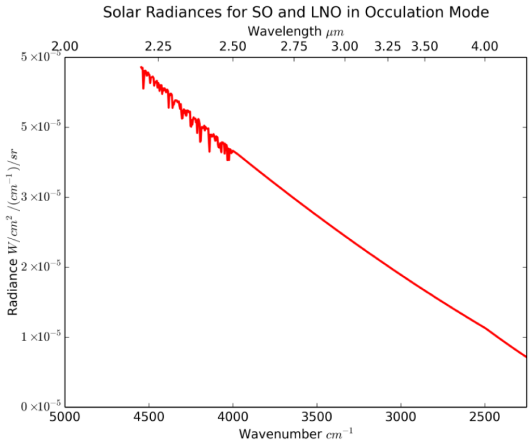

Fig. 3. Solar spectral radiance entering the SO and LNO solar occultation apertures. Note that radiance is invariant with Sun-Mars distance. Below 2.5µm solar absorption lines are present in the spectrum.

#252874 Received 29 Oct 2015; revised 7 Jan 2016; accepted 8 Jan 2016; published 16 Feb 2016

3.1. Flux passing through optical components

The elements common to both the SO and LNO channels are: an AOTF, which selects the spectral interval of interest; a diffraction grating positioned in a quasi-Littrow configuration; a detector array of 320 × 256 pixels; and a series of optical elements such as mirrors and lenses, for which the transmission or reflectivity curves are known. These are described in more detail here:

AOTF bandpass filter – When a radio-frequency (RF) field is applied to the AOTF crystal, the waves induce a periodic pattern of expansion and compression within the crystal, causing a specific range of wavelengths to exit the crystal at a different angle to the main beam. By controlling the input RF, the desired wavelength range can be selected, filtering all other radiation and preventing it from reaching the diffraction grating – and therefore acting as an order sorting filter for the spectrometer. The AOTF spectral response to a broadband light source typically varies as a *sinc* function i.e. $\sin c(x) = \sin(x)/x$, where the correct RF input is chosen so that the centre wavelength of the passband corresponds to the central wavelength of the grating's FSR at the desired order, which is then diffracted onto the central pixel of the detector. The sinc function creates sidelobes which overlap into adjacent orders, though through optimising the properties and shape of the RF transducer, these out-of-band elements can be minimised. Hence, in this SNR calculation it was assumed that the transmission (as a function of wavelength) can be approximated by a Gaussian with a full-width half-maximum equal to the bandpass, as follows:

$$\tau_{AOTF}(\lambda) = \exp\left(\frac{-(\lambda-\lambda_{centre})^2}{2\left(\Delta\lambda/2\sqrt{2\ln(2)}\right)^2}\right) \quad (2)$$

Where τ_{AOTF} is the transmission of the AOTF at a wavelength λ within the diffraction order under investigation, λ_{centre} is the central wavelength of that order, and $\Delta\lambda$ is the bandwidth of the AOTF for that diffraction order.

AOTF efficiency - The AOTF has a non-uniform spectral response, and the efficiency of the crystal also depends on the angle of the incoming beam, so the radiation entering the instrument is diffracted by the AOTF with a slightly different efficiency depending on the angle of incidence. Therefore for each wavelength within the chosen diffraction order, the total radiation passing through to the slit and grating is a sum of the product of the AOTF bandpass filter shape [Eq. (2)], transmission efficiency of the optical path at this wavelength [Fig. 4], and the normalized efficiency of the AOTF at this angle of incidence [Fig. 5].

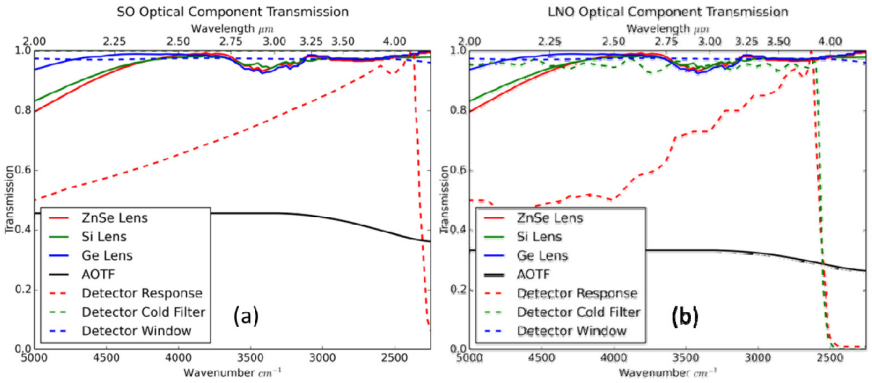

Fig. 4. Transmission properties of the optical components in the SO (a) and LNO (b) channels.

#252874 Received 29 Oct 2015; revised 7 Jan 2016; accepted 8 Jan 2016; published 16 Feb 2016

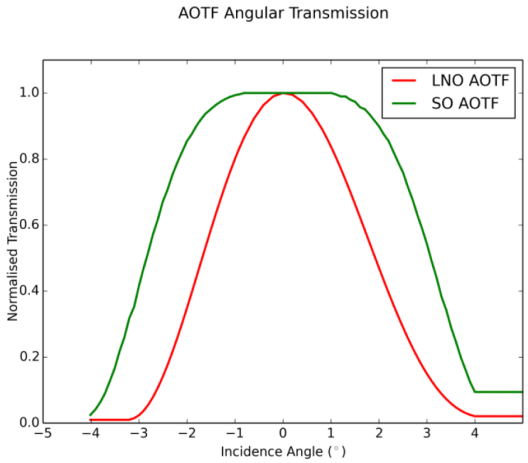

Fig. 5. AOTF transmission efficiency versus angle of incidence. NOMAD's AOTF has been positioned so that the on-axis photons pass through the center of the AOTF and hit the center of the detector with minimal attenuation. The LNO AOTF is much larger than the SO AOTF, which increases throughput but results in a higher attenuation of off-axis light.

Grating dispersion – One diffraction order is selected by the AOTF: radiation within this passband passes through to the slit and onto the echelle grating, which diffracts the radiation through further optics and onto the detector according to Bragg's Law. As the angle of diffraction depends on the wavelength, each detector pixel in the horizontal (spectral) direction will receive a different wavelength of radiation. The dispersion of radiation towards each pixel is dependent on the properties of the grating, such as blaze function, groove density and orientation with respect to the other optical components. The blaze function [Fig. 6] is the wavelength-dependent diffraction efficiency within one order, which peaks at 1 in the centre of the order (detector pixel 160).

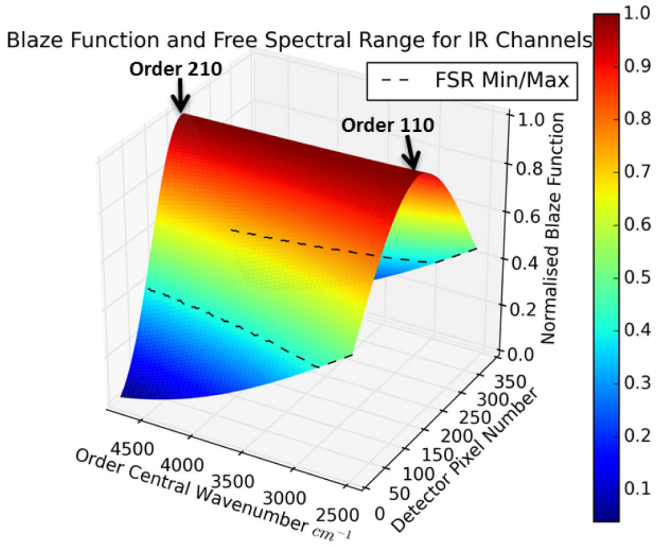

Fig. 6. Blaze function and Free Spectral Range parameters for the SO and LNO channels. A measurement of one order corresponds to a horizontal slice across the entire detector at a single central wavenumber. The blaze function peaks in the centre of the detector for all diffraction orders, but the fall-off varies with order (and central wavenumber of that order). The grating's FSR varies non-linearly with order also; therefore pixels below the dotted line contain adjacent orders and are omitted from the calculation. At low orders, the FSR is larger than the detector; hence some small spectral ranges cannot be measured.

#252874 Received 29 Oct 2015; revised 7 Jan 2016; accepted 8 Jan 2016; published 16 Feb 2016

Detector properties – After the optics, the final element in each optical chain is the detector, which consists of a silicon window, behind which sits a cooled detector array. The window is attached to the exterior, hence remains at a similar temperature as the instrument. For the LNO channel, it was necessary to block as much of the radiation forming the thermal background as possible. Therefore in the LNO detector there is also a cold filter, which is cooled down to the same temperature as the detector element. In the calculation, the spectral response of the window and filter has been considered, plus the spectral responsivity and 75% efficiency of the detector in converting received photons to electrons (i.e. the quantum efficiency).

3.2. Differences between SO and LNO channels

There are a few small but important differences between the optical components in the SO and LNO channels. These are described in detail elsewhere [5], but are summarised here:

- Firstly, in nadir mode, a flip mirror is placed in the LNO optical path. When in solar occultation mode, the beam reflects off two additional mirrors, but not the flip mirror. The SO channel has only one viewing port, reflecting always off two mirrors, instead of a flip mirror.
- The AOTF in the LNO channel is larger than in SO and has a slightly larger spectral bandwidth (24 cm^{-1} vs. 22 cm^{-1}).
- The LNO slit is 4 pixels wide and 150 pixels high, whereas SO is 2 × 30 pixels. The increased width increases the throughput at the expense of spectral resolution, and the increased height means that the Instantaneous Field Of View (IFOV) is larger, again to increase the photon flux in nadir mode. Note that in occultation mode, the Sun does not fill the increased IFOV of the LNO channel – instead, it should subtend ~20 pixels (in the vertical, spatial direction) of the LNO detector, as in SO, depending on the angular size of the Sun when viewed from Mars. In normal operation, to maximize SNR, 144 illuminated spatial pixels are binned during each nadir observation; during occultation however, a binning factor of 6 is more typical, so that some spatial information can be retained to achieve a higher spatial resolution IFOV.
- Some of the optical components present have slightly different transmission properties, particularly the LNO detector, which contains a cold filter which cuts off at 3.8μm (rather than the 4.3μm of SO) and a larger AOTF with reduced transmission efficiency. A comparison of the two channels is shown in Fig. 4.

3.3. Flux incident on detector

The signal arriving on the detector can be expressed as:

$$S(\lambda) = \frac{a\pi}{4\left(F/\#\right)^2}\Delta\lambda W_{slit}\tau_{opt}(\lambda)R(\lambda) \tag{3}$$

where *F/#* is the channel's F-number, a is the area of one detector pixel, $\Delta\lambda$ is the pixel spectral bandwidth, W_{slit} is the slit width, $R(\lambda)$ is the incoming radiance, and $\tau_{opt}(\lambda)$ is the transmission of the optics. This latter variable is a product of the transmission properties of all optics: mirrors, lenses, AOTF ($\tau_{AOTF}(\lambda)$ and angular dependency), and echelle grating blaze function. The model calculates the flux for one diffraction order at a time, therefore any pixels that receive a flux outside the grating's FSR are ignored, as they are accounted for in an adjacent order. The number of electrons $S(i)$ generated in a detector pixel i during integration time Δt is given by:

#252874 Received 29 Oct 2015; revised 7 Jan 2016; accepted 8 Jan 2016; published 16 Feb 2016

$$S_{electrons}(i) = \frac{\lambda_i}{hc} \tau_{det}(\lambda_i) E_Q(\lambda_i) S(\lambda_i) \Delta t \quad (4)$$

where λ_i is the wavelength corresponding to the pixel *i*, *h* is Planck's constant, *c* is the speed of light, $E_Q(\lambda)$ is the quantum efficiency of the detector and $\tau_{det}(\lambda)$ is the sensitivity of the detector at the given wavelength, including responsivity, cold filter transmission and detector window transmission.

3.4. Detector noise consideration

Different sources of noise need to be considered:

- **Read-out noise** N_{ro} originates from the detector and the readout electronics, and is a fixed source of noise, measured in electrons per pixel per observation. For the MARS MW detector in the SO and LNO channels, this has a value of 1000 e^-/pixel.
- **Dark current noise** N_{dark} is also a fixed source of noise, measured in electrons per pixel per second. The dark current is 6000 e^-/pixel/s, therefore the noise is assumed to be $N_{dark} = \sqrt{6000 \Delta t}$ in each of the IR channels, where Δt is the integration time.
- **Thermal background shot noise** N_{tb} is the noise in the detector produced by the thermal background, calculated as $N_{tb}(i) = \sqrt{S_{tb}(i)}$ where $S_{tb}(i)$ is the electrons generated in detector pixel *i* due to thermal emission coming from the instrument.
- **Quantization noise** N_{quant} is due to the finite number of bits (*nbits* = 14 for SO and LNO) for encoding the signal detected by the detector chip. It is calculated as:

$$N_{quant} = \frac{S_{FWC}(i)}{\sqrt{12}.2^{nbits}\left(\frac{V_{ADC\max} - V_{ADC\min}}{V_{ADC}}\right)} \quad (5)$$

where $S_{FWC}(i)$ is the full well capacity of detector pixel *i*, $V_{ADC\max}$, $V_{ADC\min}$, correspond to the usable voltage range of the analogue-to-digital converter and V_{ADC} is the converter's maximum voltage range. For NOMAD, $S_{FWC}(i) = 37\text{x}10^6$, $V_{ADC\max} = 4.06\text{V}$, $V_{ADC\min} = 0.28\text{V}$ and $V_{ADC} = 5\text{V}$.

- **Shot noise** N_{shot} is the noise resulting from the signal photons impacting the detector, where $N_{shot} = \sqrt{S_{electrons}(i)}$.

3.5. Thermal background estimation

For an instrument at a temperature of 263-283K, the thermal background makes the largest contribution to the noise, increasing the thermal background shot noise, particularly in nadir viewing mode where the signal is much lower than when viewing the sun. All the mechanical and optical components within the instrument act as blackbody radiation sources, emitting thermal photons; some of which can reach the detector. The total thermal background is difficult to calculate, since all elements that could radiate must be included in the analysis, and depending on their position in the optical chain, their emitted radiation passes through different numbers of elements. The cold filter in the LNO detector limits the field of view, so that thermal emission incident on the detector must have passed through the optical chain. Emission was reduced as much as possible by using very highly transmissive lenses (>0.95 across most of the spectral range) and highly reflective mirrors (>0.95) so that the slit and diffraction grating are the primary sources of thermal emission. It was assumed that emissivity = 1 – reflectance in the calculation, and the slit was assumed to have an emissivity of 0.99 All components are assumed to be at the same temperature as the instrument, except for the cold filter and detector, which are assumed to be at their operating temperature of 85K

#252874 Received 29 Oct 2015; revised 7 Jan 2016; accepted 8 Jan 2016; published 16 Feb 2016

within the detector housing. The optical components are attached to a thermally conductive baseplate inside NOMAD - away from the heat-generating central electronics boards – so the temperature of the parts should not deviate by more than a few degrees from the main instrument body.

The calculation is run for each detector pixel individually, split into three parts: contributions from optical components before the AOTF, from the AOTF to the slit, and after the slit. Due to the limited bandpass of the AOTF and the low emissivity (high transmission/reflectance) of the mirrors and lenses, the first part is very small, but is included for completeness. The second part makes a larger contribution as the AOTF itself has a higher emissivity, and because photons emitted here are diffracted by the grating at all diffraction orders, hence the contributions from every order must be added together. The grating diffracts the thermal photons however, distributing them across the detector array - unlike the emission from the grating itself and the optics after the grating, which is directly incident on each pixel. Therefore this final part provides the greatest contribution.

Thermal emission is modelled using the Planck blackbody equation, which determines the power emitted per unit area per unit of solid angle of a component's surface, at the given wavelength λ and temperature T:

$$B(\lambda,T)=\frac{2hc}{\lambda^5}\frac{1}{\exp\left(hc/\lambda k_B T\right)-1} \tag{6}$$

where k_B is the Boltzmann constant. The number of electrons generated in the detector by emission of wavelength λ from surface n is therefore:

$$S_{electrons,n}(\lambda,T_n)=\varepsilon_n(\lambda)B(\lambda,T_n)\left(\lambda/hc\right)A\Omega\left(\prod_{j=n+1}^{m}\tau_j(\lambda)\right)E_Q(\lambda)\Delta t \tag{7}$$

where $\varepsilon(\lambda)$ is the surface emissivity, $\left(\lambda/hc\right)$ is the energy of one photon, $A\Omega$ is the etendue as viewed by a detector pixel, $\prod_{j=n+1}^{m}\tau_j(\lambda)$ is the cumulative transmission of all m optical elements between the surface and the pixel, $E_Q(\lambda)$ is the quantum efficiency of the detector, and Δt is the observation time. To first approximation, the signal in electrons in detector pixel i by thermal emission from before the AOTF can be calculated as follows, summed over the n optical components before the AOTF:

$$S_{tb1}(i)=\sum_n\left(\frac{S_{electrons,n}(\lambda_{i+1},T_n)+S_{electrons,n}(\lambda_i,T_n)}{2}\right)\left(\lambda_{i+1}-\lambda_i\right) \tag{8}$$

For those components between the AOTF and the slit, the calculation becomes more complex, as all diffraction orders x need to be accounted for:

$$S_{tb2}(i)=\sum_n\sum_{x=0}^{\infty}\left(\frac{S_{electrons,n}(\lambda_{x,i+1},T_n)+S_{electrons,n}(\lambda_{x,i},T_n)}{2}\right)\left(\lambda_{x,i+1}-\lambda_{x,i}\right) \tag{9}$$

Finally, for the grating and components after the slit, the signal in electrons is simply:

$$S_{tb3}(i)=\sum_n\int_{\lambda=0}^{\infty}S_{electrons,n}(\lambda,T_n) \tag{10}$$

And therefore, for each pixel i the total thermal background in electrons $S_{tb}(i)$ can be calculated by adding the three components $S_{tb1}(i)$, $S_{tb2}(i)$, and $S_{tb3}(i)$.

#252874 Received 29 Oct 2015; revised 7 Jan 2016; accepted 8 Jan 2016; published 16 Feb 2016

3.6. SNR calculation

The total noise on pixel *i*, when measuring diffraction order *x*, is given by:

$$N(i,x) = \sqrt{N_{dark}^2 + N_{ro}^2 + N_{quant}^2(i,x) + N_{shot}^2(i,x) + N_{tb}^2(i,x)} \tag{11}$$

So, substituting the relevant variables and values, the SNR can be written as:

$$\frac{S(i,x)}{N(i,x)} = \frac{S_{electrons}(i,x)}{\sqrt{6000\Delta t + 1000^2 + \left(\frac{S_{FWC}(i,x)}{\sqrt{12}.2^{nbits}\left(\frac{V_{ADC\max} - V_{ADC\min}}{V_{ADC}} \right)} \right)^2 + S_{electrons}(i,x) + S_{tb}(i,x)}} \tag{12}$$

The AOTF transmission efficiency has an angular dependence [Fig. 5], therefore pixels away from the centre of the detector receive less signal. The model accounts for this by calculating the signal and noise for each illuminated detector pixel for each order.

The calculation then diverges between the occultation and nadir viewing geometries: for occultation, the SNR is very high, hence spatial and temporal resolution are maximised considering the SNR of each pixel individually, by not binning or co-adding consecutive pixels. In reality, data rate limitations prevent the transmission to Earth of data from every pixel; however the instrument is highly programmable, therefore presenting all possible binning and co-addition schemes would not be feasible here.

On the other hand, for nadir, SNR values are low and therefore must be maximised at the expense of spatial and temporal resolution. The signal and noise values derived for all 144 illuminated pixels are summed to generate a column-binned SNR for that observation of the diffraction order under investigation. To further increase the SNR, consecutive observations are co-added, to fill a pre-defined observation period, which is set at 15s for this study (a single 15s observation is not possible, as the thermal background would saturate the detector). NOMAD's nadir observation strategy is also highly flexible, and will therefore be adapted over time to optimise science return.

4. Results

4.1. Integration times

A suitable integration time must be chosen so that the detector is not saturated by the signal and thermal background incident on it. For this study, optimal integration times were calculated using the model described, which are given in Fig. 7 for typical SO, LNO solar occultation and LNO nadir observations. In this ideal case, we chose to define an optimal integration time that included a small margin to avoid saturating the detector: hence these times correspond to a 95% saturation of the detector. As described previously, a single observation period is either 1s or 15s in duration, and therefore the number of co-added observations is calculated to fit within this period (rounded down to the nearest whole number). For example, from Fig. 7, the optimal integration time is 1000ms, when NOMAD is at 263K, and LNO is measuring at 2500cm^{-1} in nadir. This means that in 1000ms, the detector is 95% saturated by the total of the signal and instrument thermal background – and therefore 15 consecutive observations can be made in one 15s observation period. The observed signal varies with wavenumber, and therefore the integration time also varies. This effect is much more pronounced in solar occultation measurements, because the signal is much larger than the thermal background, and hence a longer integration time can be used at wavenumbers where the instrument's transmission is lower.

#252874 Received 29 Oct 2015; revised 7 Jan 2016; accepted 8 Jan 2016; published 16 Feb 2016

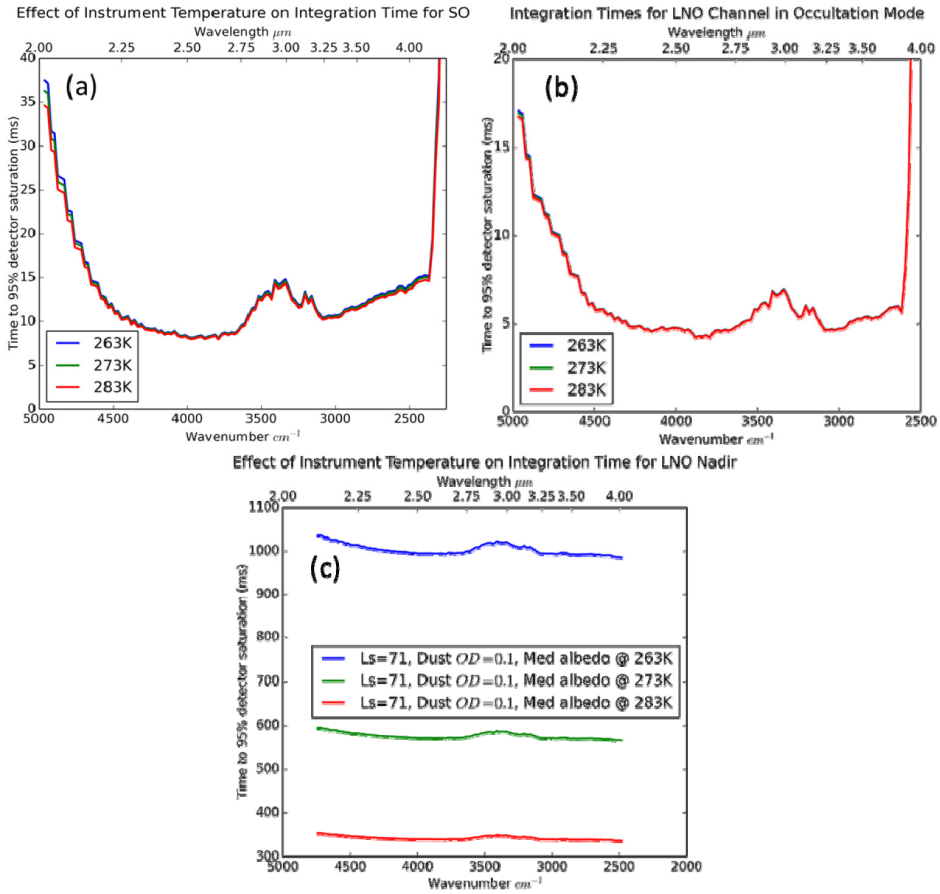

Fig. 7. Integration times for the SO (a), LNO solar occultation (b) and LNO nadir (c) channels at 263K, 273K and 283K. In nadir mode, the thermal background is an order of magnitude larger than the signal from Mars; therefore the integration time is mainly dependent on instrument temperature. In occultation mode, the solar flux dominates the thermal background; hence the change with temperature is very small.

4.2. Solar occultation observations

The results of the calculations for both the SO channel and the LNO channel in solar occultation mode are presented in Fig. 8. SNRs of 5000-6000 are expected for both channels in occultation mode within their nominal spectral ranges. The short-wavelength cutoff below 2.2μm is not accurately modelled here, as it largely depends on the RF driver being able to deliver a high power output at high frequencies, which it was not designed to do. A lower RF power will reduce the AOTF diffraction efficiency significantly, and during nominal science operations measurements will not usually be made below 2.2μm to avoid stressing the RF driver.

#252874 Received 29 Oct 2015; revised 7 Jan 2016; accepted 8 Jan 2016; published 16 Feb 2016

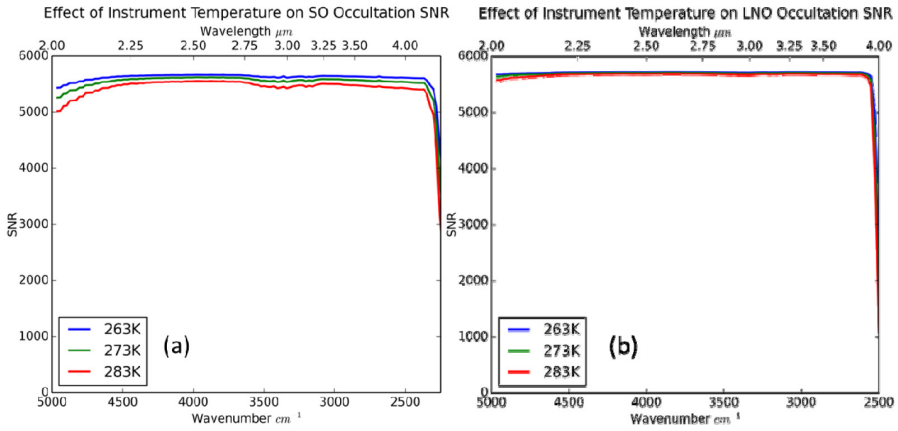

Fig. 8. Expected SNRs for SO (a) and LNO occultation (b) observations for three instrument temperatures (263K, 273K and 283K).

4.3. Nadir observations

In total, 144 model runs were performed: for each of the three instrument temperatures, there are four solar zenith angles or dust opacities, each with three albedo cases, and each of these for two Sun-Mars distances. It is not feasible to present all 144 cases, therefore selected results are shown here only in Fig. 9, Fig. 10, Fig. 11 and Fig. 12. A wide range of SNR values has been derived, typically between 20 in the worst-case scenarios and 160 in the best. Solar zenith angle appears to have the greatest effect, where a change from 0° to 80° results in a greater-than-fourfold reduction in SNR. The change in flux between perihelion and aphelion also has a strong effect, reducing SNRs by approximately a third. Similarly, a change from high to medium albedo results in a decrease of around a quarter. Increasing dust opacity actually increases the SNR, due to higher radiances being reflected from the atmosphere, rather than being absorbed by the surface.

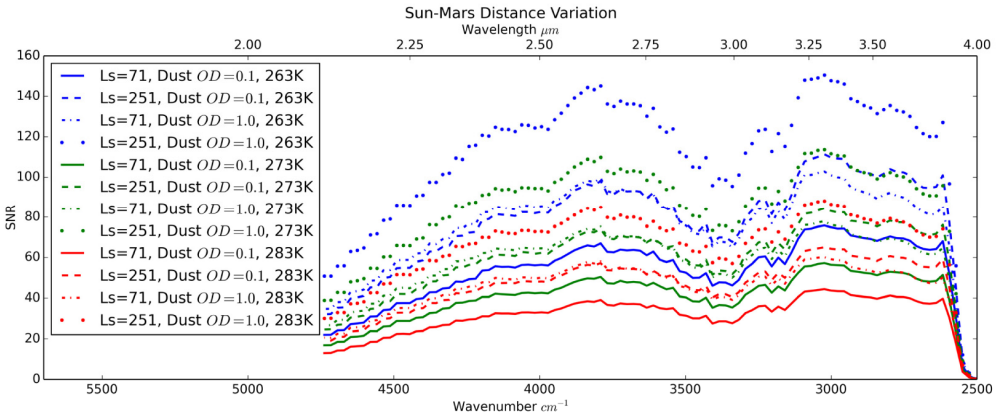

Fig. 9. Effects of Sun-Mars distance variations: Expected SNR for LNO nadir observations for one solar zenith angle (45°), two dust cases (OD = 0.1 and OD = 1), intermediate surface albedo (0.242), two Sun-Mars distances (1.38AU @ L_s = 251° and 1.67AU @ L_s = 71°) and three instrument temperatures (263K, 273K and 283K).

#252874 Received 29 Oct 2015; revised 7 Jan 2016; accepted 8 Jan 2016; published 16 Feb 2016

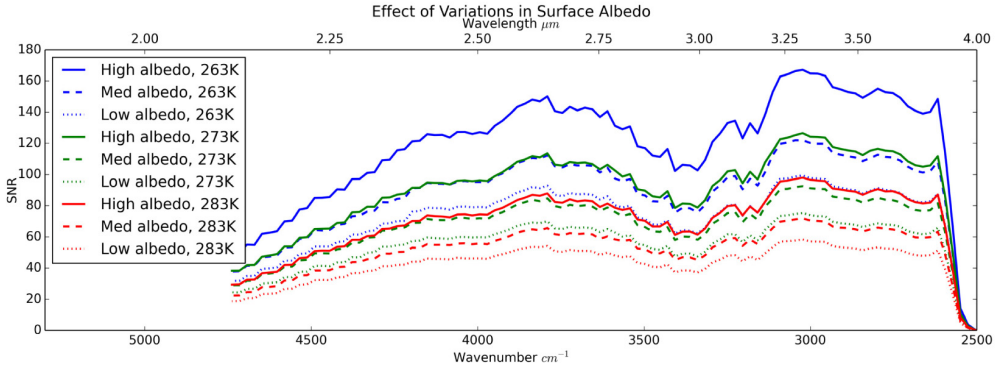

Fig. 10. Effects of Variations in Albedo: Expected SNR for LNO nadir observations for one solar zenith angle (45°), one dust case (OD = 0.4), three surface albedos (0.179, 0.242 and 0.361), one Sun-Mars distance (1.38AU @ L_s = 251°) and three instrument temperatures (263K, 273K and 283K).

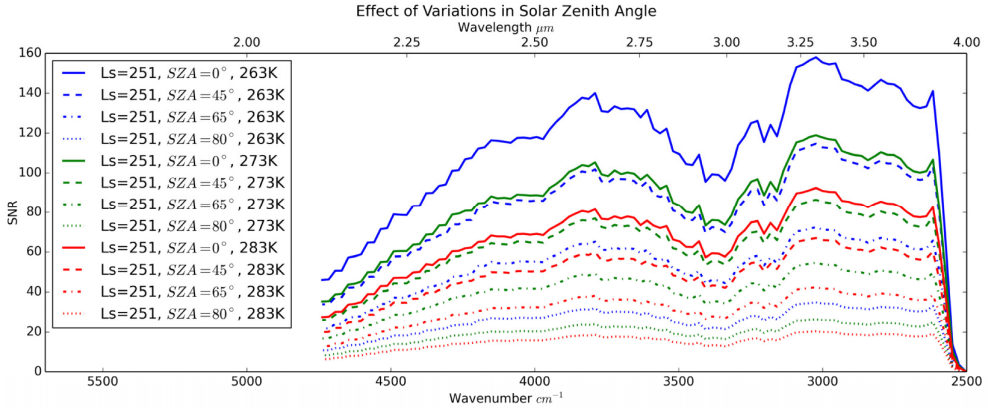

Fig. 11. Effects of Variations in Solar Zenith Angle: Expected SNR for LNO nadir observations for four solar zenith angles (0°, 45°, 65° and 80°), one dust case (OD = 0.2), intermediate surface albedo (0.242), one Sun-Mars distance (1.38AU @ L_s = 251°) and three instrument temperatures (263K, 273K and 283K).

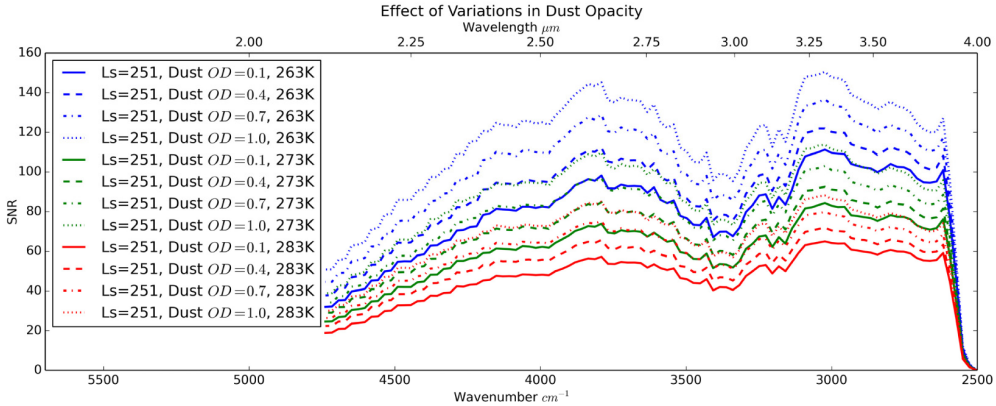

Fig. 12. Effects of Variations of Dust Opacity: Expected SNR for LNO nadir observations for one solar zenith angle (45°), four dust cases (OD = 0.1, 0.4, 0.7, 1.0), intermediate surface albedo (0.242), one Sun-Mars distance (1.38AU @ L_s = 251°) and three instrument temperatures (263K, 273K and 283K).

#252874 Received 29 Oct 2015; revised 7 Jan 2016; accepted 8 Jan 2016; published 16 Feb 2016

5. Conclusions

NOMAD is a suite of three spectrometers that will be launched in 2016 as part of the joint ESA-Roscosmos ExoMars Trace Gas Orbiter mission. The instrument is a combination of three channels that cover the IR and UV spectral ranges and can perform solar occultation, nadir and limb observations, to detect and map a wide variety of Martian atmospheric gases and trace species. Another paper [1], published separately, described the optical and radiometric modelling work performed for the UVIS channel. In this second part, we have described the optical models representing the two IR channels, and used them to determine signal to noise levels for many expected observational cases.

This study shows that the instrument will be capable of measuring a suite of gas species that are or could be present in the atmosphere of Mars in both viewing modes. The solar occultation technique is a very powerful observational method: it is self-calibrating (the Sun is viewed directly at the beginning or end of the occultation period, depending on ingress or egress, as a reference spectrum), enabling the retrieval of vertical profiles of the target molecules from the upper layers of the atmosphere down to the surface (or near-surface depending on the loading in dust and particles). Solar occultations have limited durations and spatial coverage on Mars, therefore nadir observations complement these, mapping a series of constituents across much more of the surface so that atmospheric sources and sinks can be investigated, and thus constraints on surface processes can be determined.

Typical LNO nadir-viewing SNRs measured in the study range from ~20, when solar zenith angles are lowest and NOMAD is hot, up to >160 in regions where the surface albedo is high and NOMAD is cold. If all conditions are favourable (dust opacity = 0.1, Mars at perihelion, Sun directly overhead, surface albedo high and NOMAD at 263K) then theoretically, SNRs ~250 can be achieved, however the likelihood of all conditions being ideal is low. For SO and LNO in solar occultation mode, SNRs are much higher, up to 5000 on condition that an optimal integration time is chosen. Therefore, this study shows that the descope of the cryo-radiator will not prevent NOMAD from achieving its intended goals in nadir mode - and has had negligible impact on solar occultation observations. With such high SNRs, sub-ppb levels of methane are still detectable by the instrument in solar occultation mode; even in nadir, the instrument has a methane sensitivity of the order of 10s of ppb assuming an average SNR of 100 [10].

Although this analysis was performed using a SNR model utilising all available data regarding optical component properties, expected instrument temperatures, and a range of anticipated atmospheric properties, this remains a theoretical exercise that will be thoroughly evaluated once ground or in-flight NOMAD calibration data is received - and eventually assessed with respect to the true performance of the instrument throughout the course of the science mission around Mars.

Acknowledgments

The NOMAD instrument is led by the Belgian Institute for Space Aeronomy (IASB-BIRA, Brussels), assisted by Co-PI teams from Spain (IAA/CSIC, Granada), Italy (IAPS/INAF, Rome) and the United Kingdom (Open University, Milton-Keynes). Associated teams contributing to the design and development of NOMAD were CSL (Liège, Belgium) and IDR-UPM (Madrid, Spain). We thank all engineering and supporting personnel in these teams. Several industrial partners were associated to the abovementioned teams. The industrial efforts were coordinated by a Belgian prime contractor (OIP, Oudenaarde). The UVIS channel has been developed at Lambda-X (Nivelles, Belgium).

NOMAD has been made possible thanks to funding by the Belgian Science Policy Office (BELSPO) and financial and contractual coordination by the ESA Prodex Office. The research was performed as part of the “Interuniversity Attraction Poles” programme financed by the Belgian government (Planet TOPERS). UK funding is acknowledged under the UK Space Agency grant ST/I003061/1. The authors would also like to thank Dennis Nevejans and the anonymous reviewers for their suggestions and improvements.

#252874 Received 29 Oct 2015; revised 7 Jan 2016; accepted 8 Jan 2016; published 16 Feb 2016

[†]**The NOMAD team – Science team**: PI: Vandaele, Ann Carine. Co-PIs: Lopez Moreno, Jose Juan; Bellucci, Giancarlo; Patel, Manish; The other members are, in alphabetical order are: Allen, Mark; Altieri, Francesca; Aoki, Shohei; Bolsée, David; Clancy, Todd; Cloutis, Edward; Daerden, Frank; Depiesse, Cédric; Fedorova, Anna; Formisano, Vittorio; Funke, Bernd;, Fussen, Didier; Garcia-Comas, Maya; Geminale, Anna; Gérard, Jean-Claude; Gillotay, Didier; Giuranna, Marco; Gonzalez-Galindo, Francisco; Ignatiev, Nicolai; Kaminski, Jacek; Karatekin, Ozgur; Kasaba, Yasumasa; Lefèvre, Franck; Lewis, Stephen; López-Puertas, Manuel; López-Valverde, Miguel; Mahieux, Arnaud; Mason, Jon; McConnell, Jack(†); Mumma, Mike; Neary, Lori; Neefs, Eddy; Novak, Robert; Renotte, Etienne; Robert, Séverine; Sindoni, Giuseppe; Smith, Mike; Thomas, Ian R.; Trokhimovsky, Sacha; Vander Auwera, Jean; Villanueva, Geronimo; Whiteway, Jim; Willame, Yannick; Wilquet, Valerie; Wolff, Mike - **Technical team**: Alonso-Rodrigo, Gustavo; Aparicio del Moral, Beatriz; Barzin, Pascal; BenMoussa, Ali; Berkenbosch, Sophie; Biondi, David; Bonnewijn, Sabrina; Candini, Gian Paolo; Clairquin, Roland; Cubas, Javier; Delanoye, Sofie; Giordanengo, Boris; Gissot, Samuel; Gomez, Alejandro; Zafra, Jose- Jeronimo; Leese, Mark; Maes, Jeroen; Mazy, Emmanuel; Mazzoli, Alexandra; Meseguer, Jose; Morales, Rafael; Orban, Anne; Pastor-Morales, Maria del Carmen; Perez-Grande, Isabel; Ristic, Bojan; Rodriguez-Gomez, Julio; Saggin, Bortolino; Samain, Valérie; Sanz Andres, Angel; Sanz, Rosario; Simar, Juan-Felipe; Thibert, Tanguy.

#252874 Received 29 Oct 2015; revised 7 Jan 2016; accepted 8 Jan 2016; published 16 Feb 2016